Numerical simulation of the slipstream and aeroacoustic field around a High-Speed Train

Zhu, Chunli; Hemida, Hassan; Flynn, Dominic; Baker, Christopher; Liang, Xifeng; Zhou, Dan

DOI:
10.1177/0954409716641150

Numerical simulation of the slipstream and aeroacoustic field around a High-Speed Train

Chunli Zhu[1, 2], Hassan Hemida[2], Dominic Flynn[2], Chris Baker[2], Xifeng Liang[1], Dan Zhou[1]

[1]Key Laboratory of Traffic Safety on Track, Central South University, People's Republic of China.

[2]School of Engineering, University of Birmingham, UK.

Abstract

The flow field and sound propagation around a three coach 1/8th scale high-speed passenger train were obtained using a detached-eddy simulation (DES) and the Ffowcs-Williams and Hawkings (FW-H) acoustic analogy. The Reynolds number of flow based on the train height and speed was 2,000,000. The numerical results of the flow and aeroacoustic fields were validated using wind tunnel experiments and full-scale data, respectively. Features of overall sound pressure level (OASPL), sound pressure level (SPL) and A-weighted SPL of typical measuring points are discussed. Sound propagated by a high-speed train is shown as a broadband spectrum concluding tonal component, where high SPLs are concentrated on the low frequency range from 10 Hz to 300 Hz. The inter-carriage gap is found to cause distinct tonal noise in contrast to the other parts of the train that cause a broadband noise. The negative log law has been used to study the influence of distance from the centre of track (COT) on the SPL, where a good fit is shown at low frequency ranges. The peak values of A-weighted SPL from both full-scale experiment and simulation results occur at

approximately 1 kHz, where simulation results show almost the same range as the experiment. Each surface of the components of the train as well as the whole train are chosen as the integral surface for the FW-H computation of the far-field noise characteristics. It was found that the sound source generated by a high-speed train is mainly dipole and the largest noise was obtained from the leading bogie. The results of this paper provide, for the first time, a better understanding of the aeroacoustic field around a three-coach train model and the paper has the potential to assist engineers in better designing high-speed trains for aeroacoustic noise reduction.

Key words

High-speed trains, train aerodynamics, aeroacoustics, DES, FW-H acoustic analogy

1. Introduction

High speed railways have undergone significant development during the last five decades since the first line was launched in Japan in 1964. Trains running at high speed (more than 250 kph) offer convenient inter-city travel but at such speeds aerodynamic effects such as drag, associated slipstreams and noise become increasingly significant. Indeed, the issues of energy efficiency [1, 2, 3] safety [4, 5, 6] and noise generation [7, 8, 9, 10, 11] are being addressed by various research groups around the world.

The methods used to investigate these issues are full-scale measurements, wind tunnel tests and numerical simulations. Full-scale testing provides realistic

data, and avoids issues associated with reduced Reynolds' number, which occur in model-scale testing [12]. Results from full-scale testing are usually averaged over several runs in order to understand the influence of environmental uncertainties and run-to-run variability [13]. However, full-scale testing is expensive and difficult due to manpower requirements, measurement equipment and obtaining line access.

On the other hand, the conditions of the model-scale tests can be more easily controlled than those in full-scale tests. However the effect of train motion on the aerodynamic force coefficients is not considered due to the stationary vehicles, which are often used in wind tunnel tests [4]. Furthermore, boundaries of a test section (solid, partially open and completely open) also have a great influence on the measurements of vehicles in a wind tunnel [14]. Computational fluid dynamics (CFD) has the capability to omit external influences on the flow (such as ambient winds) but CFD is also not easy to handle due to the large length/height ratio of high speed trains that requires specialised techniques and expertise [13]. Although CFD can offer a more detailed result, large mesh sizes and small time-steps can cause simulations to become prohibitively expensive. Like all numerical models, CFD requires validation against physical experiments. Therefore, CFD offers a more detailed view of the flow field when used in conjunction with physical experiments.

There are different CFD techniques available to researchers, some of them are scale-resolving techniques, which provide information about the instantaneous flow field, such as Direct Numerical Simulations (DNS),

large-eddy simulation (LES) and DES. Alternatively, Reynolds Averaged Navier-Stokes (RANS) method provides a description of the mean flow. However, due to the strong dependence of a RANS solution on the chosen turbulence model (which are scarcely calibrated to bluff body flows), RANS has difficulty in the prediction of complex separated unsteady flows [15]. Methods such as DES and LES are becoming popular approaches for solving the instantaneous flow phenomena around ground vehicles [16, 17, 18, 19]. Hemida et al. [16] and Krajnović et al. [17] used LES to investigate the effect of platform height on the slipstream of high speed trains and flow around a bus-shaped body, respectively. In their work, fine spatial resolution in the near wall region is required, which makes LES computationally expensive and rarely practical for the complex engineering applications. DES uses LES to resolve the detached flow and an Unsteady Reynolds Averaged Navier-Stokes (URANS) model is used within the boundary layer. The switch between URANS and LES is based on the model length scale and grid spacing [20]. Flynn et al. [18] and Muld et al. [19] utilised the S-A model for the delayed detached-eddy simulation (DDES) approach for studying the slipstream of a freight train and a simplified high speed train. Although the DES approach based on the k-ε model shows superior performance over the original DES method [21] based on S-A model it has not yet been used in the study of train aerodynamics. Many variants on the k-ε model are the standard k-ε model, the RNG k-ε model and a realizable k-ε model, referred as SKE, RNG and RKE below, respectively. Lateb et al. 's work [21] illustrated the problems of the SKE model when reproducing flow-field structures, while RNG and RKE yielded the

best agreement with wind tunnel tests [22]. RKE model based DES approach provided by commercial code FLUENT has been used in this paper, because of its effectiveness in transporting turbulence quantities [23].

Aerodynamic and aeroacoustic problems are a major limitation factor in the speed-up of trains on railway networks [24]. Noise induced by high-speed trains can cause adverse physical, physiological and psychological effects on humans, which is a matter of continuing concern [7, 8]. The aerodynamic noise generated by a turbulent flow increases with the eighth power of the velocity [25]. Therefore, aeroacoustic problems caused by trains become more significant at higher speeds and consequently affect people near railway lines.

Experimental methods including full-scale tests [9, 26, 27], wind tunnel tests [9, 28, 29, 30]and computational simulations [31, 32, 33] are the main methods in the research of the aeroacoustic features of high speed trains. Besides the high cost of full-scale tests mentioned above, it is not easy to distinguish sound sources accurately [10]. It is equally difficult to determine the independent contribution of each noise source [34] (rolling noise, aerodynamic noise, and traction noise [11]) to the total noise of a running high-speed train. Additionally, due to the varying environment as well as absorption and reflection by the surroundings, the mechanism of noise propagation to the far field cannot be fully studied. Aeroacoustic results from wind tunnel experiments can be detrimentally affected by low frequency pulsation of inlet flow and high levels of background noise [35]. Computational simulation of aeroacoustic noise can be performed using the FW-H acoustic analogy for the prediction of aeroacoustic noise from a moving

surface [36]. This method has gained growing attention in recent years for the flow-induced noise prediction[37, 38, 39]. For high-speed train related issues, Zhu et al.[40] and Yu et al.[41] used the FW-H acoustic analogy to study the noise produced by a 1/10th scale isolated simplified wheelset model and isolated pantograph system. From their study the SPL, OASPL, A-weighted SPL as well as noise directivity were analysed for the individual components of train. Sun et al.[33] used a nonlinear acoustic solver and the FW-H model to study aeroacoustic field generated by a high-speed train. Pressure measurements such as probes on the surface of the train have been used to calculate aeroacoustic fields but little work has been done with far-field computation. This paper is an example of far-field propagation, noise distribution and noise directivity calculated using the results from CFD simulations.

In this paper, a DES/FW-H aeroacoustic simulation has been performed to elucidate the slipstream behaviour, as well as aeroacoustic field, around a high speed passenger train. The structure of this paper is organised as follows. Computational Methodology is described in Section 2, experimental setup is shown in Section 3. Computational details are given in Section 4. Aerodynamic results are analysed in Section 5 and the aeroacoustic analysis is performed in Section 6. Conclusions are drawn in section 7.

2. Computational Methodologies

2.1 DES

RKE model based DES has been extensively validated for a wide range of

flows, including boundary layer flows and separated flows [22]. This method separates the models in the two-layer approach by use of a damping function to smooth the transition between URANS and LES [42]. The transport equations of this model are:

$$\frac{\partial}{\partial t}(\rho k)+\frac{\partial}{\partial x_j}(\rho k u_j)=\frac{\partial}{\partial x_j}[(\mu+\frac{\mu_t}{\sigma_k})\frac{\partial k}{\partial x_j}]+G_k+G_b-\rho\varepsilon-Y_M+S_k \quad (1)$$

$$\frac{\partial}{\partial t}(\rho \varepsilon)+\frac{\partial}{\partial x_j}(\rho \varepsilon u_j)=\frac{\partial}{\partial x_j}[(\mu+\frac{\mu_t}{\sigma_{\grave{o}}})\frac{\partial \varepsilon}{\partial x_j}]+\rho C_1 S\varepsilon-\rho C_2\frac{\varepsilon^2}{k+\sqrt{v\varepsilon}}+C_{1\varepsilon}\frac{\varepsilon}{k}C_{3\varepsilon}G_b+S_\varepsilon \quad (2)$$

where the model constants are $C_{1\varepsilon}$=1.44, C_2=1.9, σ_k=1.0 and $\sigma_{\grave{o}}$=1.2; G_k and G_b represent the generation of turbulence kinetic energy due to the mean velocity gradients and buoyancy, respectively. The model turbulent viscosity μ_t is obtained from the turbulent kinetic energy k and the rate of dissipation of kinetic energy ε as Eq. (3).

$$\mu_t=\rho C_\mu\frac{k^2}{\varepsilon} \quad (3)$$

The dissipation term in RKE is modified as:

$$Y_k=\frac{\rho k^{\frac{3}{2}}}{l_{des}} \quad (4)$$

where $l_{des}=\min(l_{\tau ke},l_{les})$, $l_{\tau ke}=\frac{k^{\frac{3}{2}}}{\varepsilon}$ and $l_{les}=C_{des}\Delta$. Δ is the maximum local grid spacing $(\Delta x,\Delta y,\Delta z)$. The model constant is taken as C_{des}=0.61 [43]. More details can be seen in ANSYS Fluent Documentation [42].

2.2 FW-H acoustic analogy

Sound is a series of pressure fluctuations propagating through compressible air. An acoustic analogy can be used to obtain aeroacoustic field data after the completion of instantaneous incompressible flow computation. This makes it possible to solve incompressible Navier-Stokes equations for the flow field at low Mach numbers and still obtain the sound propagation. The acoustic analogy used in this paper is based on the FW-H approach, in which the complete solution consists of a surface integral to included monopole and dipole noise sources whilst the boundaries and volume integrals include quadrupole sources [44]. The differential form of the FW-H equation can be written as [45],

$$(\frac{1}{c_0^2}\frac{\partial^2}{\partial t^2}-\nabla^2)p^{'}=\frac{\partial}{\partial t}\{[\rho_0 v_n+\rho(u_n-v_n)\delta(f)]\}-\frac{\partial}{\partial x_i}\{[P_{ij}n_j+\rho u_i(u_n-v_n)]\delta(f)]\}+\frac{\partial^2}{\partial x_i\partial x_i}[T_{ij}H(f)] \quad (5)$$

where c_0 and ρ_0 are the sound speed and density in a quiescent medium, respectively; $\delta(f)$ is the Dirac delta function; u_n is the fluid velocity component normal to the integration surface, v_n is the surface velocity component normal to the surface; $p^{'}$ is the sound pressure at far-field that can be defined as,

$$p^{'}=p-p_0 \quad (6)$$

T_{ij} is the Lighthill stress tensor, which is written as,

$$T_{ij}=\rho u_i u_j+p_{ij}-c_0^2\rho\delta_{ij}$$

7)

$H(f)$ is Heaviside function described as,

$$H(f)=\begin{cases}0, \textit{ for } f<0\\ 1, \textit{ for } f>0\end{cases} \quad 8)$$

The three types of aeroacoustic noise sources, monopole, dipole and quadrupole can represent fluctuations in the fluid mass within a given volume, fluctuating force and fluctuating stress, respectively [44]. For high speed trains, monopole noise can be neglected on the condition that the train's surface is supposed to be rigid wall [46]. The ratio between the total sound power of quadrupole and the total sound power of dipole is proportional to the Mach number squared [47]. Thus, for the exterior noise of high speed train which operated at low Mach number, the quadrupole term can be ignored and the dominant sources are more typically dipole-type sources [32, 44].

3. Experimental configuration

3.1 Wind tunnel experiment (Aerodynamic Part)

Wind tunnel experiments were carried out in the second test section of the CARDC (China Aerodynamic Research and Development Centre), which is an 8x6 m low-speed wind tunnel with a closed test section. The second test section has length, width and height dimensions of 16.1 m, 8 m and 4.94 m, respectively, whilst the effective cross-sectional area is 39.2 m^2. A 360°rotating turntable is installed in the middle of the wind tunnel with a diameter of 7 m to simulate the train operating at different yaw angles to the wind. Ground simulation has a

strong influence on the flow field as well as the measurement of drag and lift coefficients on the train [5]. Single track ballast and rail (STBR) configuration with a stationary floor was applied in the tests shown in **Figure 1**(a) [48]. The fixed ground plate was mounted 1.06 m above the wind tunnel floor to minimise the influence of the boundary layer on the wind tunnel floor on the train. The STBR configuration's leading and trailing edges were angled to reduce the disturbance to the oncoming flow. The schematic of wind tunnel is shown in **Figure 1(b)**. The boundary layer thickness above the floor in the empty wind tunnel was found to be less than 20 mm, which means that the quality of the flow field is essentially uniform at the position of the fixed ground plane. The mean inflow velocity used in the wind tunnel experiment was u_{in} =60m/s. Electronic pressure scanner valves were used for the measurement of the surface pressures on the train whereas a six-component balance system was used to measure the forces. A detailed description of the experimental work can been found in Zhang et al. [6].

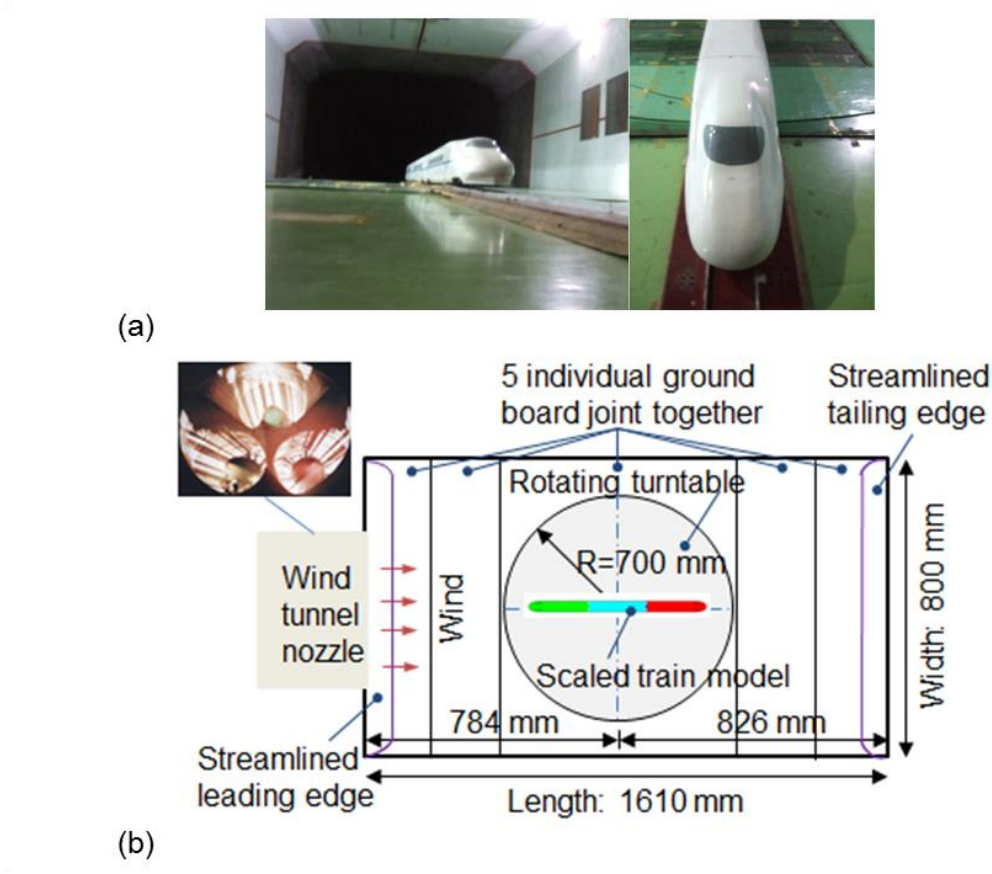

Figure 1. Wind tunnel experiment: (a) train model; (b) schematic of wind tunnel.

3.2 Full-scale experiment (Aeroacoustic Part)

Full-scale experiments were carried out on the high-speed train line from Nanchang to Yichun where the experimental setup is shown in Figure 2(a). When a train passed the position of microphone array, the microphones started collecting data by initiating devices synchronously and continuously. The wheel-phased microphone array with 11 rods is shown in Figure 2(b), has the capability to restrain side lobe. Noise distribution was obtained by the phase comparison method of each time segment. Non-negative least squares (NNLS)

method was taken for data post processing, where the number of iteration time was 100. The test equipment consisted of 66 1/4 inch microphones, a microphone calibrator and a related data collecting and post processing system. The microphone array was installed 19 m from COT, 3.5 m from top of rail (TOR). The distance between initiating devices and centre of microphone array was 15 m. Results of full-scale experiment described in this paper are A-weighted SPL to 1/3 octave band at speed of approximately 67m/s.

(a) (b)

Figure 2. Full-scale experiment: (a) site arrangement; (b) wheel phased microphone array.

4. Computational Setup

4.1 Computational model

High-speed trains are usually operated in multi-car sets. An example is the commercial CRH2 train which usually runs with 8 or 16 coach sets. Muld et al [19] studied the effect of different train lengths on the flow structures in the wake and illustrated strong similarities between the wake structures regardless of the number of coaches. Therefore it can be concluded that the slipstream behaviour

of a 3 car train is representative of that on the first 2 cars of an 8 car train set. Figure 3 shows the 1/8th scale computational model and integral surfaces used in this paper. The model has a full-scale length, width and height dimensions of 76 m, 3.68 m and 3.36 m, respectively. The dimensions in this paper are given as full-scale values in order to allow the reader to compare the results to real-world cases. The scaled train model used both in the wind tunnel experiments and CFD are separated into the lead car, middle car and tail car. Simplified bogies were included and the fairing structure around the inter-carriage gaps was also kept in the model.

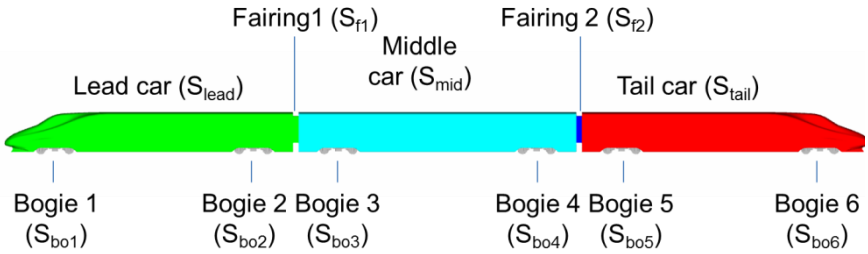

Figure 3. Computational model and each integral surface.

4.2 Computational domain and boundary conditions

Figure 4 shows the computational domain and boundary conditions used in the present work. The x, y and z axes are along the train's length, width and height directions, respectively. The origin is denoted as being at the front face of the train (x), COT (y) and TOR (z), in accordance with CEN [51]. For the aerodynamic assessment of a high speed train, the CEN [5149] recommendations state that the inlet of the computational domain should be at least 8 characteristic heights (H) upstream, and 16 H downstream of the model, where

H is the height of the train from the TOR.

In order to obtain a more accurate comparison between the wind tunnel tests and the CFD simulations, the width and height of the computational domain were specified to match those of the wind tunnel. However, the length was chosen according to CEN [49], which is longer than that of the wind tunnel's test section to guarantee the wake flow was fully-developed and reduce any effect of the boundary conditions on the flow around the train. The computational domain has a length of 68H in the streamwise direction, a width of 17H and a height of 11H. Train model was installed at the same distance of 8.5H from centreline of train to the sidewalls similar to the experiment. The inlet boundary is 14H upstream of and the outlet is at 34H downstream of the train. Based on these dimensions, the blockage ratio is below 5% including the blockage due to STBR, which complies with CEN [49]. Based on the characteristic height of the train and the freestream velocity (u_{in} =60m/s), the Reynolds number of the flow around the train model is 2,000,000. As the Mach number in this study is only 0.18, the flow can be considered to be incompressible. Inlet was set as a velocity inlet with a steady uniform profile of u_{in}=60m/s. The outlet was set as a zero-pressure outlet. The ground was set as the moving ground which is differs from the ground of wind tunnel which has a stationary ground. However, because the wind tunnel has measures to control the boundary layer on ground as described before, the more realistic case of setting the velocity the same as the inlet (u_{in}) is applied. The surface of train was set as a no-slip wall along with other boundaries which were

also set as no-slip walls to match the closed-jet wind tunnel.

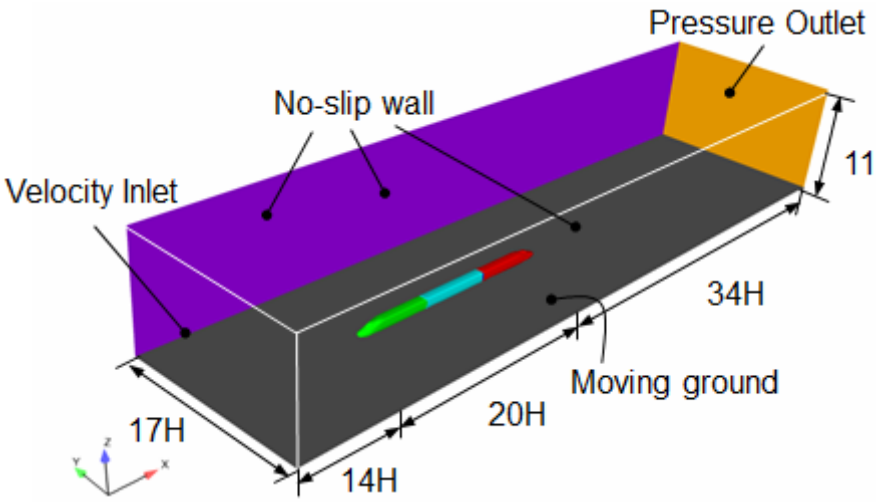

Figure 4. Computational domain and boundary conditions.

4.3 Computational mesh

Unstructured hexahedral grids were built using snappyHexMesh, which is an automatic meshing utility within OpenFOAM 2.3.0. Three meshes were made for the mesh sensitivity study. The coarse mesh, medium mesh and fine mesh consisted of 21 million cells, 36 million cells and 65 million cells, respectively. In all cases the maximum skewness of the cells was below 3. The mesh was dominated by hexahedral cells although due to the complexity of the train's geometry, a small number of polyhedral cells were also present. Figure 5 shows the surface mesh of the train nose, bogie, fairing and the longitudinal cross-section at y=0 m of the fine mesh.

(a) (b)

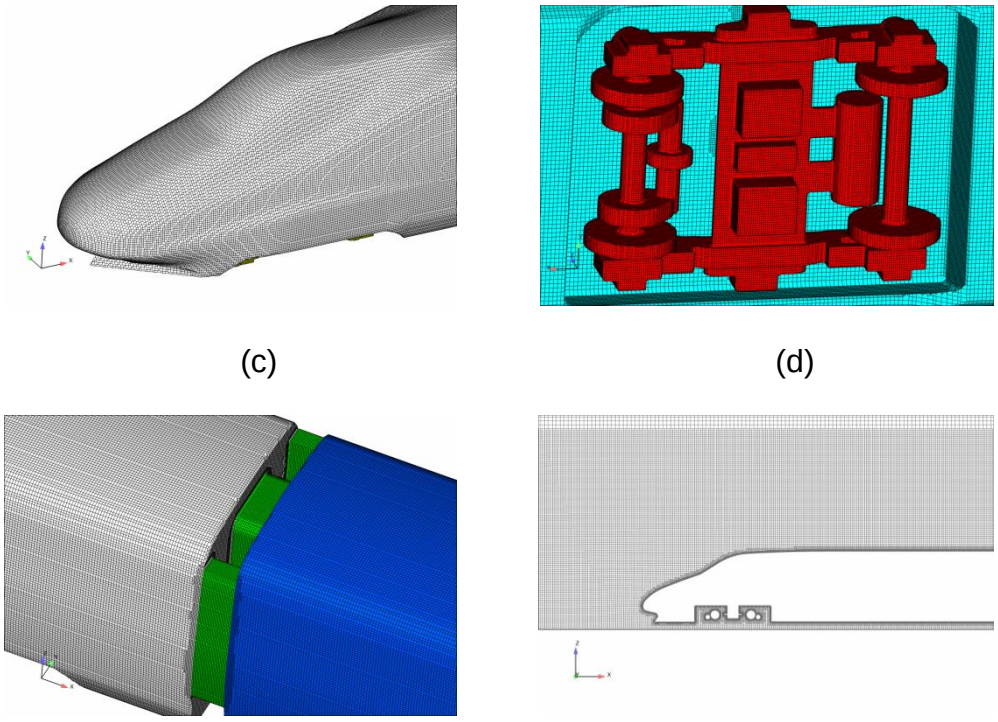

Figure 5. Fine mesh: (a) nose area; (b) bogie area; (c) fairing; (d) cross-section at y=0 m.

Turbulent flows are significantly affected by the presence of walls and the near-wall modelling impacts on the fidelity of numerical solutions. For this reason, accurate representation of the flow in the near-wall region is an important factor in the accurate prediction of wall-bounded turbulent flows. Mesh quality in the near wall region is important in running DES, otherwise an improper switch from RANS modelling to LES could cause modelled-stress depletion and leading to grid-induced separation [20]. Table 1 shows the dimensionless wall distance (y^+) for different meshes obtained from the RKE model based DES simulations, which is the criterion for the FLUENT to switch between the linear viscous layer

law and the turbulent logarithmic wall law. The y^+ value is calculated by:

$$y^+ = \frac{yu^*}{v} \quad (9)$$

where u^* is the friction velocity, y is the distance between the first node and the train surface in the wall normal direction, and v is the kinematic viscosity. More information about enhanced wall treatment used by the RKE model based DES model can be seen in ANSYS FLUENT Documentation [42].

Table 1. The dimensionless wall distance (y^+) for different meshes.

Mesh	Cells (x10^6)	y^+ max	y^+ average
Coarse	23	50.7	36.8
Medium	41	32.4	17.9
Fine	65	31.5	16.8

4.4 Numerical setup

The simulations were conducted using the commercial CFD code Fluent 6.3. The SIMPLEC scheme was used to decouple the velocity and pressure terms. Pressure was discretised using second order central differencing, while the convection term was discretised using Bounded Central Differencing. The turbulent kinetic energy and turbulent dissipation rate were also discretised using second order central differencing scheme. To aid stability of the DES, a steady RANS solution was used to calculate an initial flow field. In the DES, time-steps were set at 0.0001 s. In total, 30,000 time steps were calculated. The convergence criteria of the absolute residuals were chosen as 10^{-6}.

In the aeroacoustic analysis, the far-field noise is computed using the FW-H analogy from the resolved flow field described in section 6. The data from 10,000 time steps (which is equivalent to 1 second of physical time) was exported to the acoustic source with a write frequency of 1 step. An incompressible solver is used because surface pressure is properly predicted for acoustic analogy at low Mach number and the volume integral is neglected in the resolution of density-based formulation of FW-H predictions 50. Different integration surfaces shown in Figure 3 as well as the entire surface of train were selected to analyse the OASPL, SPL and A-weighted SPL of typical measurement points. No far-field assumption has been made in the formulation of the FW-H analogy [50], thus receivers were all installed in the far-field at distances larger than 10 H from COT due to the limitation of the FW-H aeroacoustic analogy in obtaining near-field results.

5. Flow field

5.1 Numerical validation

DES is a combination of RANS and LES, therefore the interface between RANS and LES needs to be tested to ensure that LES is not solved inside the boundary layer. Figure 6 illustrates the variation line of u_{mag}/u_{in} and l_{des}/l_{rke} at different heights from the train roof. This shows the characteristics of boundary layer and RANS/LES interface, where u_{mag} represents the magnitude of velocity. From description in section 2.1, RANS is taken when $l_{des}/l_{rke}=1$ while LES is

taken when $l_{des}/l_{rke}<1$. In Figure 6, the non-dimensional boundary layer thickness of the coarse, medium and fine mesh solutions is 0.019, 0.013 and 0.013, respectively. The position of the interface between the RANS/LES modes of the coarse, medium and fine meshes is 0.039, 0.029 and 0.030, respectively. Therefore, all of the dimensions of the interface are larger than the boundary layer thickness, which means RANS is only applied within the boundary layer.

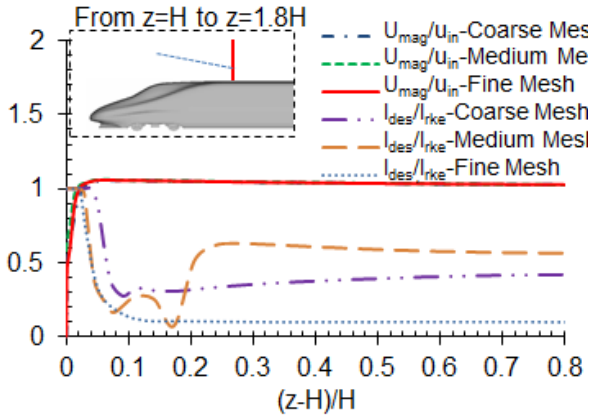

Figure 6. DES model properties of different meshes.

To ensure the accuracy of the solutions obtained from the three mesh densities with respect to the wind tunnel data, validation must be performed. The parameters used for verifying the results below are the force coefficient, pressure coefficient and slipstream velocity.

Here, the drag coefficient C_d and the lift coefficient C_l are defined as,

$$C_d = \frac{F_d}{qA} \qquad 10)$$

$$C_l = \frac{F_l}{qA} \tag{11}$$

where q is the dynamic pressure shown defined as,

$$q = \frac{1}{2}\rho u_{in}^2 . \tag{12}$$

In Eq. (10), Eq. (11) and Eq. (12), F_d and F_l represent the time-averaged drag force and lift force, respectively; ρ is the density of the freestream, A is the reference area. In order to maintain consistency with CEN[49], the experimental data and CFD data have been normalised by the standard reference area and reference length of 10 m^2 and 3 m, respectively.

Table 2. Time-averaged force coefficients validated against wind tunnel data.

Method	Mesh	Lead Car		Middle Car		Tail Car	
		C_d	C_l	C_d	C_l	C_d	C_l
CFD	coarse	0.18	-0.03	0.08	-0.01	0.16	0.10
	medium	0.16	-0.05	0.09	-0.02	0.17	0.10
	Fine	0.17	-0.06	0.09	-0.04	0.17	0.13
Wind tunnel	-	0.17	-0.05	0.09	-0.03	0.18	0.11

The time-averaged drag coefficient and lift coefficient obtained from DES cases are outlined in Table 2, in which a blockage correction has been applied to the wind tunnel results. For the boundary condition installation and mesh quality described above, drag coefficient of each train are within 11% of the wind tunnel

data. The lift forces are shown to be in reasonable agreement where results from fine grid are within 33% of the wind tunnel data. This discrepancy is believed to be due to the difference in ground simulation between CFD and wind tunnel.

Figure 7 shows the normalised slipstream velocity magnitude, U, relative to a static observer obtained from the different meshes. U is defined by

$$U = \frac{\sqrt{(u_{in} - u)^2 + v^2 + w^2}}{u_{in}} \quad 13)$$

where u, v, and w are the longitudinal, the lateral, and the vertical velocity components in the computational domain, respectively. This method converts the velocity to the frame of reference of a static observer with the train passing by [18]. Results from different meshes show little difference, hence it can be assumed that the large energy-containing motions have been resolved and the resolution of the fine mesh is sufficient for the purposes of this work. Some discrepancy in the near wake occurs between mesh densities due to the highly unsteady flow which exists there. This region is of little interest in terms of aeroacoustic behaviour so this difference is considered unimportant for this work.

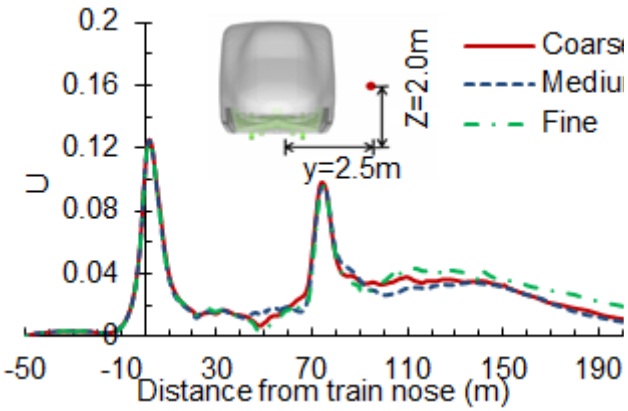

Figure 7. Mesh sensitivity studies of normalised slipstream velocity for the coarse (23 million), medium (41 million) and fine (65 million) meshes.

The surface pressure on the train is the source item for the computation of the far-field aerodynamic noise via FW-H acoustics analogy.

Figure 8 shows the mean static pressure coefficients C_p along four different rings around the cross-section of the train. C_p is defined as,

$$C_p = \frac{p - p_a}{q} \quad , \tag{14}$$

where $\boldsymbol{p}$ is the static pressure and $\boldsymbol{p_a}$ is the atmospheric pressure.

Figure 8 shows C_p on the streamlined part of head car. The small variation of C_p between each mesh is attributed to the relatively steady flow caused by the streamlined design of lead car. Apart from some difference which occurs at x=5.42 m, the CFD results of pressure distribution of different meshes were similar to those from the wind tunnel experiment. From the results described

above it can be deduced that there is no need for further mesh refinement and remaining results described in this paper are all from fine mesh.

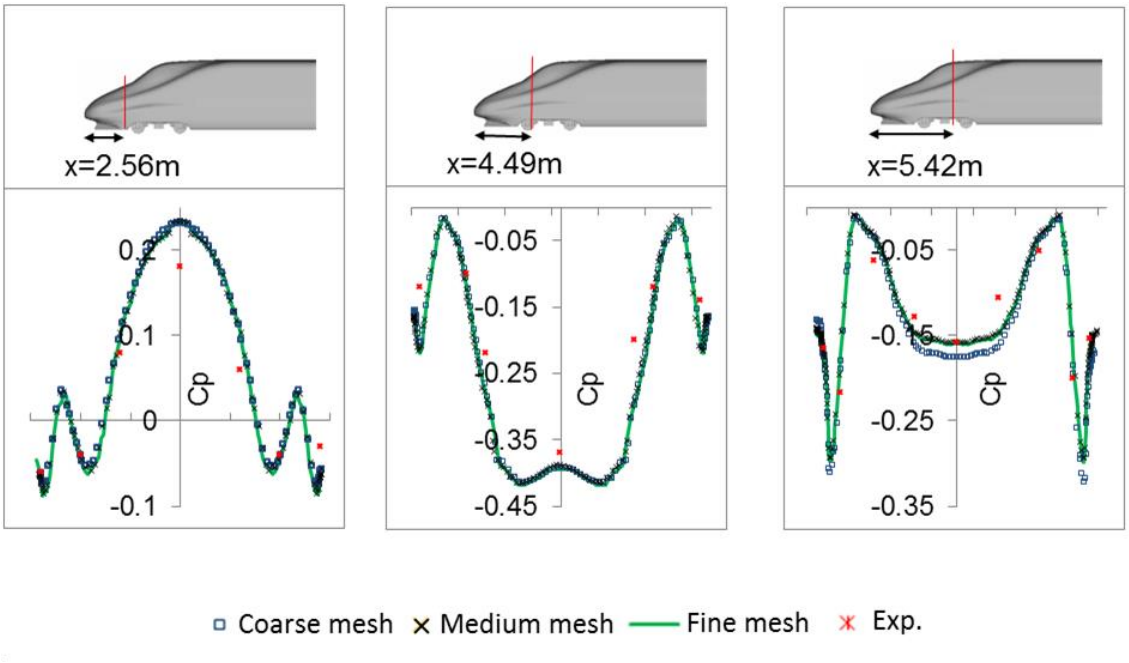

Figure 8. Mesh sensitivity test for mean pressure coefficients on train cross sections at : (a) x=2.56 m; (b) x=4.49 m; (c) x=5.42m.

5.2 Slipstream analysis

Mean and instantaneous characteristics of the slipstream are discussed in this section, where mean flow is averaged after the simulation has already reached a fully-developed state from 15,000 time-steps to 30,000 time-steps. The positions of the slipstream samples are shown in Figure 9.

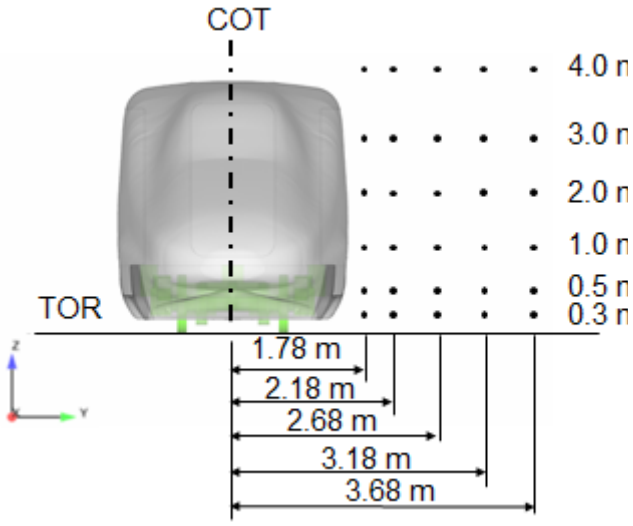

Figure 9. Measuring line of slipstream velocity and mean pressure coefficient relative to COT and TOR.

Figure 10 shows the slipstream velocity with varying distances from COT and TOR. It is observed that the general trend of higher velocities exists closer to the ground due to the increased relative roughness of the bogies in comparison to the sides and roof of the train. Variations in velocity are more significant closer to COT which are not only influenced by the train body but also by the underbody complexities such as the bogies at the two lowest heights. Moreover, in Figure 10(a) and Figure 10(b), the six velocity peaks at y=1.78 m correspond to the six bogies in sequence, respectively.

The slipstream velocity profiles show a rapid increase followed by a sharp decrease in the nose region, especially significant at lower position to TOR and nearer position to COT (Figure 10(a)). The near wake region is another area where high slipstream velocities occur. However, at distances further than 1.78

m from COT and within z=3 m from TOR, the slipstream peak value caused by the nose region exceeds the peak value in the near wake region. When the distance from COT is larger than 1.78 m, the slipstream velocities are all lower than 0.3. Similar sets of results have also been obtained using LES [52] and full-scale measurements [13, 53].

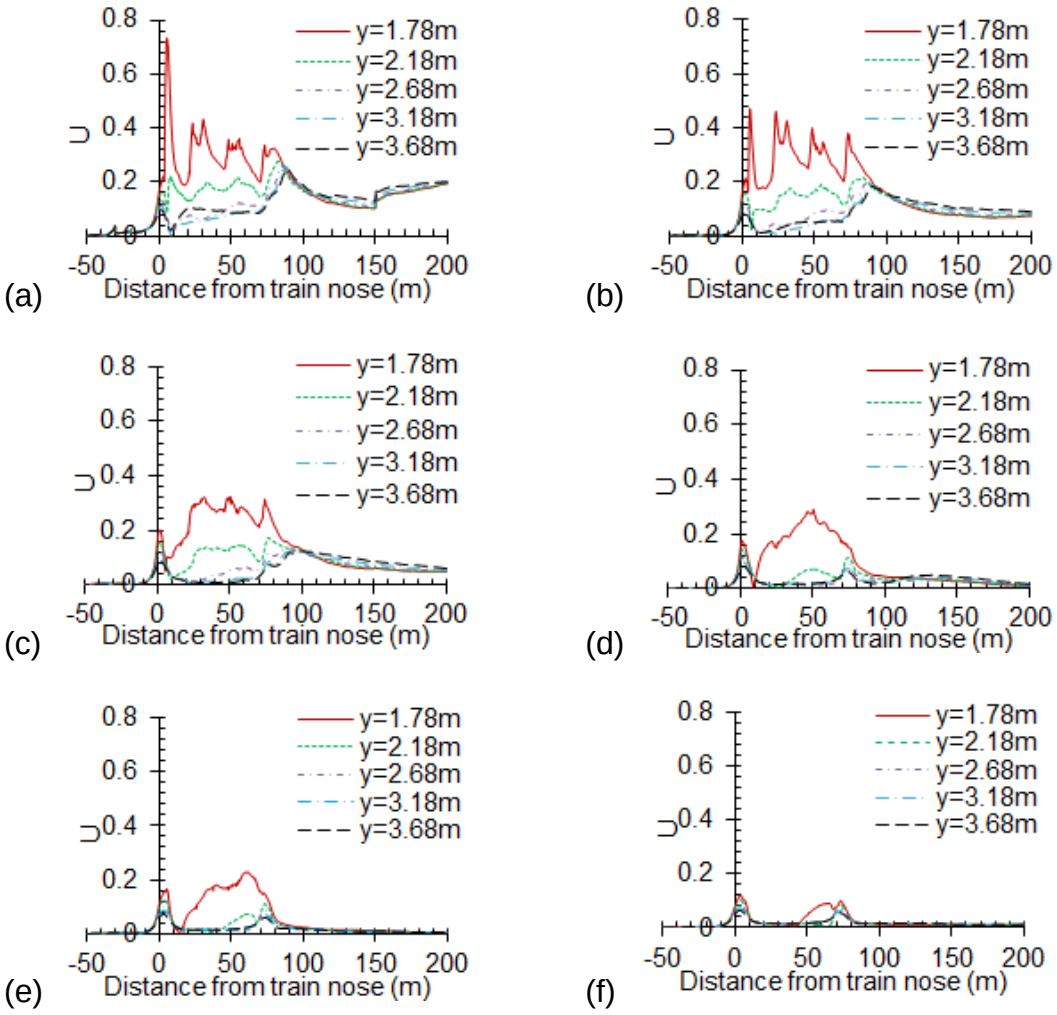

Figure 10. Slipstream velocity U at distance from the COT and varying distance above TOR: (a) z=0.3 m; (b) z=0.5 m; (c) z=1 m; (d) z=2 m; (e) z=3 m; (f) z=4 m.

Head pressure pulses due to trains passing-by are also quantified by measuring points at different position to COT and TOR (Figure 11). The pressure trace around a train is essentially characterised by a larger nose transient, minor inter-car transients and by the tail transient which is nearly the inverse shape of the nose transient. The largest peak values are shown at points of y=1.78m at height of 0.3 m from COT (Figure 11 (a)), which has a positive peak value is 0.20 whilst negative peak value -0.25.

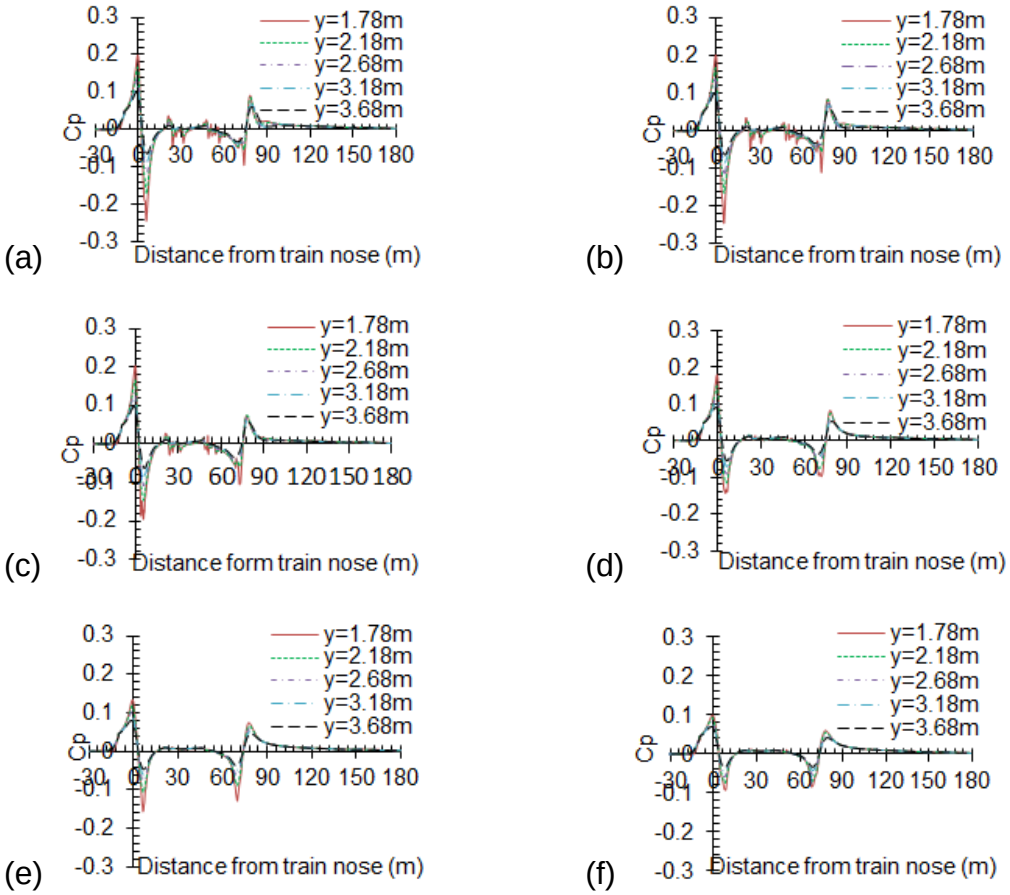

Figure 11. Mean pressure coefficient C_p at distance from the COT and varying distance above TOR : (a) z=0.3m; (b) z=0.5m; (c) z=1m; (d) z=2m;(e) z=3m;(f) z=4m.

As a method of characterising the level of turbulent fluctuations, turbulence intensity is defined as,

$$I \equiv \frac{u'}{U_{mean}} \tag{15}$$

where u' is the root-mean-square (RMS) of the velocity fluctuations and U_{mean} is the mean velocity magnitude, in this case u_{in}.

Figure 12 shows the mean turbulence intensity at different distances from COT as well as different distance from ground, where turbulence intensities larger than 20% occurred 1.8 m away from COT at height of z=0.2 m and z=0.5m. Highly unsteady flow is observed at the first two measuring positions above TOR and above COT. The most significant turbulence peaks at z=0.5m are shown in Figure 12(b). The six positions correspond to the six bogie sets. Therefore, velocity profile u_{mag}/u_{in} is analysed in Figure 13, where first bogie shows two near-symmetric peak value of u_{mag}/u_{in}, which are much larger than results obtained from other bogies.

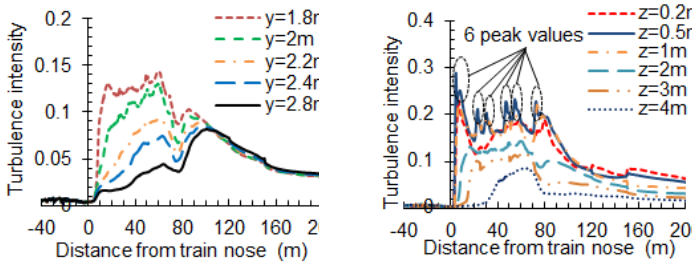

(a) (b)

Figure 12. Turbulence intensity: (a) different distance from COT (2 m from TOR); (b) different distance from ground (1.8 m from COT).

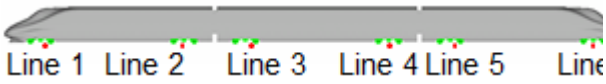

(a)

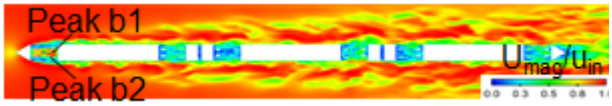

(b)

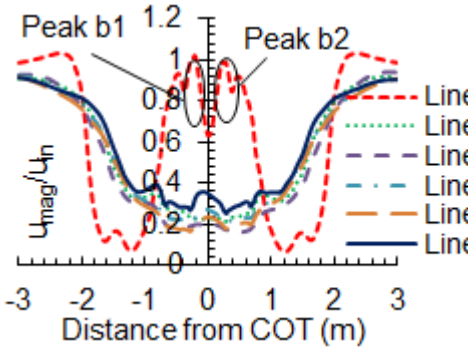

(c)

Figure 13. Velocity profile u_{mag}/u_{in} around each bogie: (a) measuring lines; (b) instantaneous velocity u_{mag}/u_{in} distribution; (c) u_{mag}/u_{in} vs. distance from COT (m).

In order to visualise the flow structures around the train, iso-surfaces of the second invariant of velocity gradient tensor, Q, was used. Q is a measurement which shows the proportion of rotation rate and shear rate of flow [55] and is defined as:

$$Q = -1/2 \partial u_i / \partial x_j \partial u_j / \partial x_i \quad (16)$$

Vortices are generated in the nose, under-floor, inter-carriage gaps and near wake regions

(

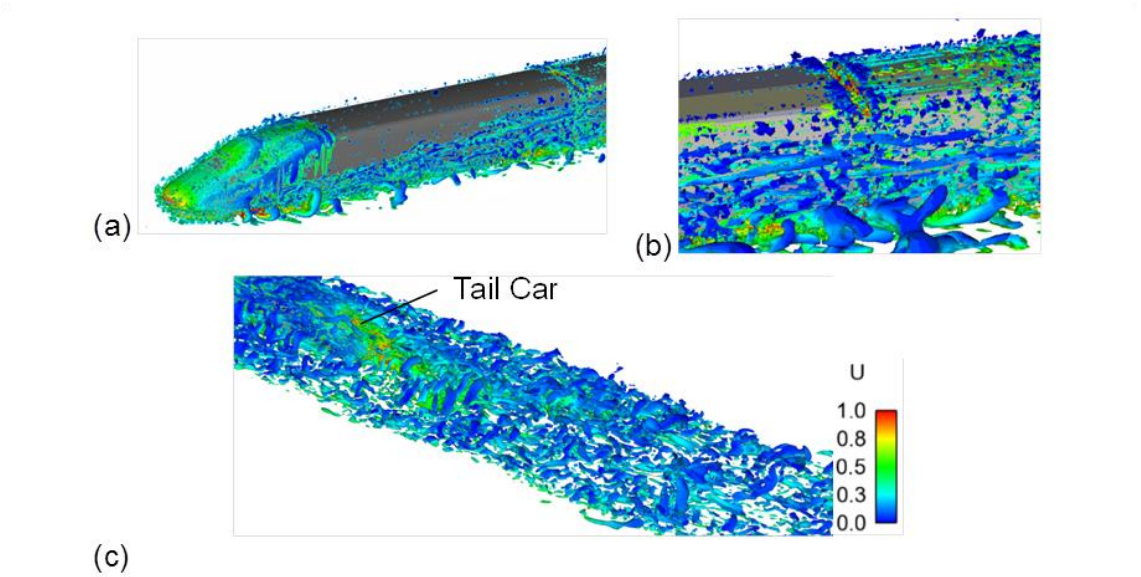

Figure 14) using iso-surfaces of Q=20,000 s-2. Small vortices are generated around the inter-carriage gaps due to the unsteady behaviour which exists there. The complicated underbody structure of the train and spatial confinement restrict the size of flow structures which emanate from beneath the train. Vortex shedding away from tail car surface formed a low pressure region as well as the flow generated underneath the train generate two strong vortices behind the train, which can also be seen in the turbulent distribution in

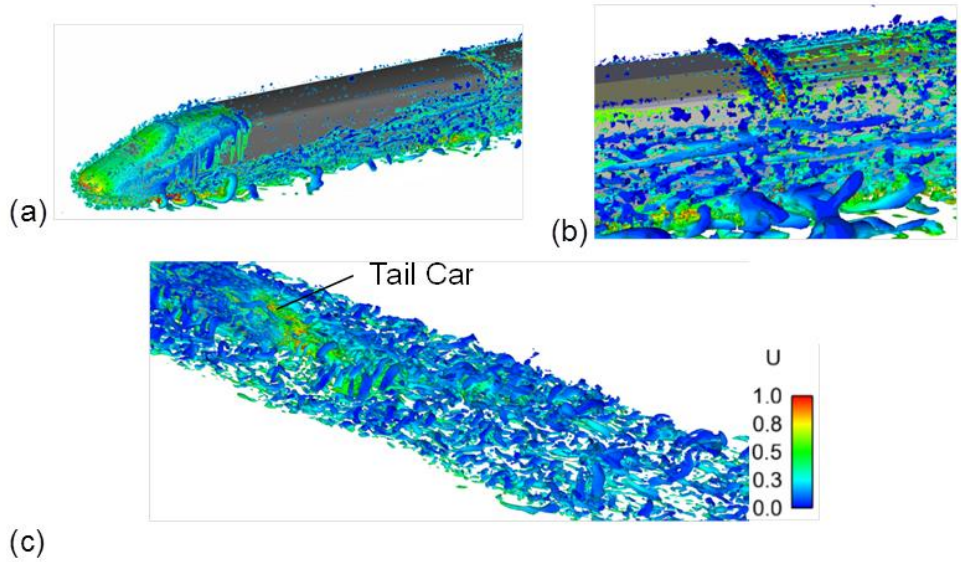

Figure 14(c).

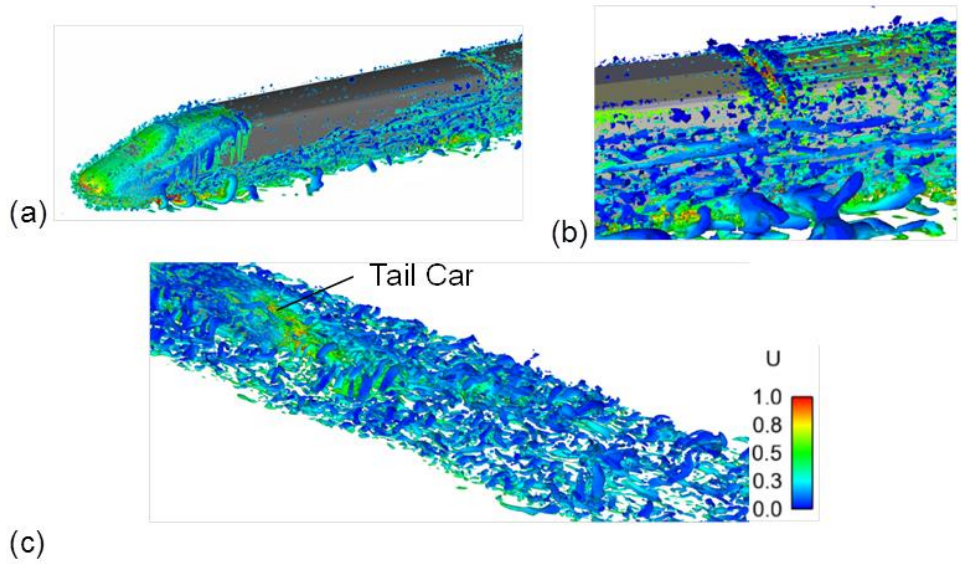

Figure 14. Instantaneous iso-surface of Q=20,000 s^{-2} coloured by slipstream velocity: (a)lead car; (b) inter-carriage gap; (c)near wake region.

6. Aeroacoustic Field

6.1 Aeroacoustic noise level in the far-field

Sound pressure is relatively low far from noise source and does not express the noise level at the position of an observer. Therefore a Fast Fourier Transform (FFT) has been used to transfer the sound pressure in the time domain into SPL in the frequency domain. All spectra are obtained by averaging Fast Fourier transforms carried out on 9,999 samples using a Hanning window. SPL, L_p, reports sound level under each specified frequency, which is defined as

$$L_p = 10\log(p(t)/p_{ref})^2 \quad (17)$$

where $p(t)$ is the RMS sound pressure in Pa; $p_{ref} = 20\mu$ Pa is the reference sound pressure [32].

Before further analysis, a mesh sensitivity study was performed using the SPL computed from S_{whole} and is shown in Figure 13. The cut-off frequency ($f_{\max}$) here is 5 kHz, which is determined by the simulation time-step: $f_{\max} = 1/(2\Delta t)$, where Δt is the time-step. From Figure 15, three meshes all showed broadband noise characteristics with the same trend that gradually decrease between 120 Hz and 250 Hz, and then become almost level but with a small negative gradient. Minor differences of the SPL profile occur between the three different meshes and are mainly concentrated on the tonal component. SPL larger than 38 dB occurs in the low-frequency range of 0-300 Hz. It is worth

mentioning that most peak values exist at a level of approximately 10Hz with respect to the high frequency broadband content of the spectrum, whilst peak SPL from three meshes are approximately 65 dB. Therefore, although containing slight discrepancies, the results from the three meshes can be considered as comparable with each other. Surface pressure results from fine mesh was chosen in the results described below.

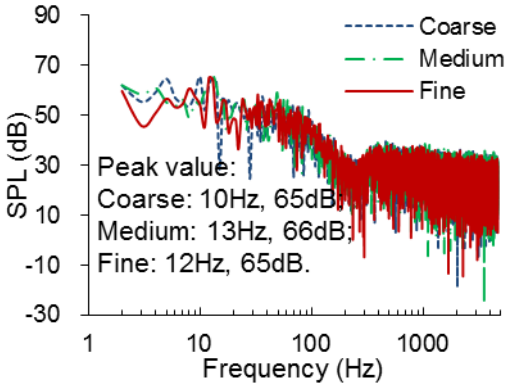

Figure 15. Mesh sensitivity study of SPL (dB) for coarse (23 million), medium (41 million) and fine (65 million) meshes (receiver installed at (5, 25, 2)).

OASPL represents an intensity of the spectrum as a whole, which provides an overall description of acoustic field. As it is a combination of all computed frequencies, it will exceed any individual SPL in the specification, where OASPL L_{pZ} (dB) is defined as,

$$L_{pZ} = 10\log[\sum_{i=1}^{n}\frac{p_i^2}{p_0^2}] = 10\log[\sum_{i=1}^{n}10^{\frac{L_{pi}}{10}}] \quad 18)$$

where p_i is the RMS sound pressure in Pa of each sound source; L_{pi}

represent single sound pressure level.

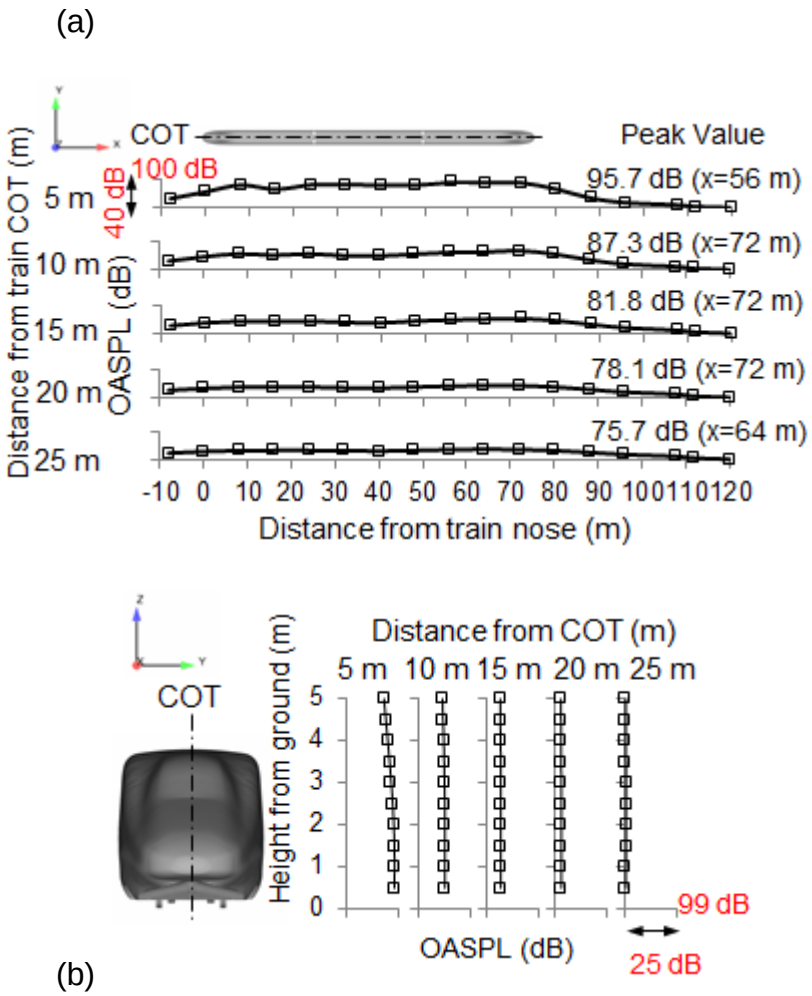

Figure 16. OASPL distribution (within 25 m from COT): (a) different distance from COT along train length at cross-sectional area of z=3.5m; (b) different distance from COT along train height at cross-sectional area of x=72 m.

Figure 16 (a) shows the variation of OASPL along the train length at z=3.5m, which is in agreement with the requirements of the EN ISO 3095 [56]. At x=8m and x=72m relatively higher OASPL occur in the nose region and near wake region,

respectively. Figure 16 (b) shows the OASPL with different height from ground at x=72m, which is where the larger OASPL values occur from Figure 16(a). In Figure 16(b), the OASPL decreases with the height from TOR and increases closer to COT. However, variation of AOSPL is not obvious when receivers are further from COT (y = 20m, 25m).

Figure 17 shows the variation of SPL with different distances from COT and TOR. In Figure 17(a), the larger distance from COT, the peak values occur at the same frequency, but exhibit an inverse trend with distance from COT. However, the influence of height on SPL is small enough, where a minor difference can be seen in Figure 16(b). The SPL profile shows the broadband noise with tonal component under some frequencies. The normal hearing range of the human ear is 20 Hz to 20 kHz, while the ear is most sensitive in the 3-4 kHz region [57]. For the 1/8th scale train model with speed of 60m/s, although OASPL is large to some extent, for example 68 dB at 25 m away from COT, the most sensitive frequency range for hearing shows low SPL level is relatively low below 40dB.

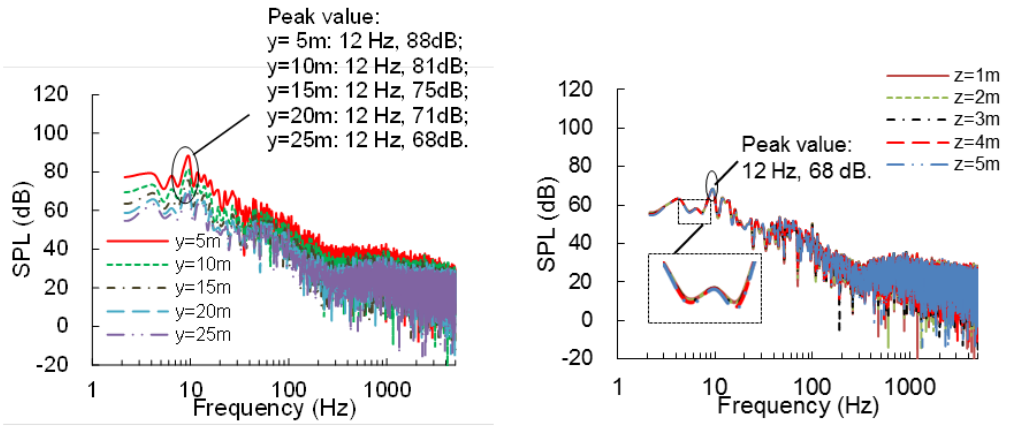

Figure 17. SPL (dB) characteristics of measuring points on plane perpendicular to TOR at x=72 m from train nose: (a) different distance from COT with height of z=5 m; (b) different distance from TOR at y=25 m from COT.

Any sound source of small dimensions can be considered as a point source for observers at great distance [58], in which corresponding logarithmic equation is described as,

$$L_p = L_{p(w)} - 20\log r - 11 \tag{19}$$

where $L_{p(w)}$ is the SPL of the source, r is the distance to the sound source.

To investigate the influence of distance from COT to SPL of a high-speed train typical frequencies of 12 Hz, 100 Hz, 1000 Hz, 4000 Hz are analysed (**Figure 18**). The purpose is to verify the entire trend of SPL attenuation with the variation of distance from COT. Negative log law curves are fitted, and the data

show good similarity at the two lowest frequencies while poor fitting occurs at 1000 Hz and 4000 Hz. The reason for the mismatch is most likely due to the complexity of the train model which is not entirely suitable to simplify as an ideal point noise source. Furthermore, the variation of SPL with distance from COT is reduced, which means noise generated at lower frequencies (100 Hz) has a larger attenuation rate.

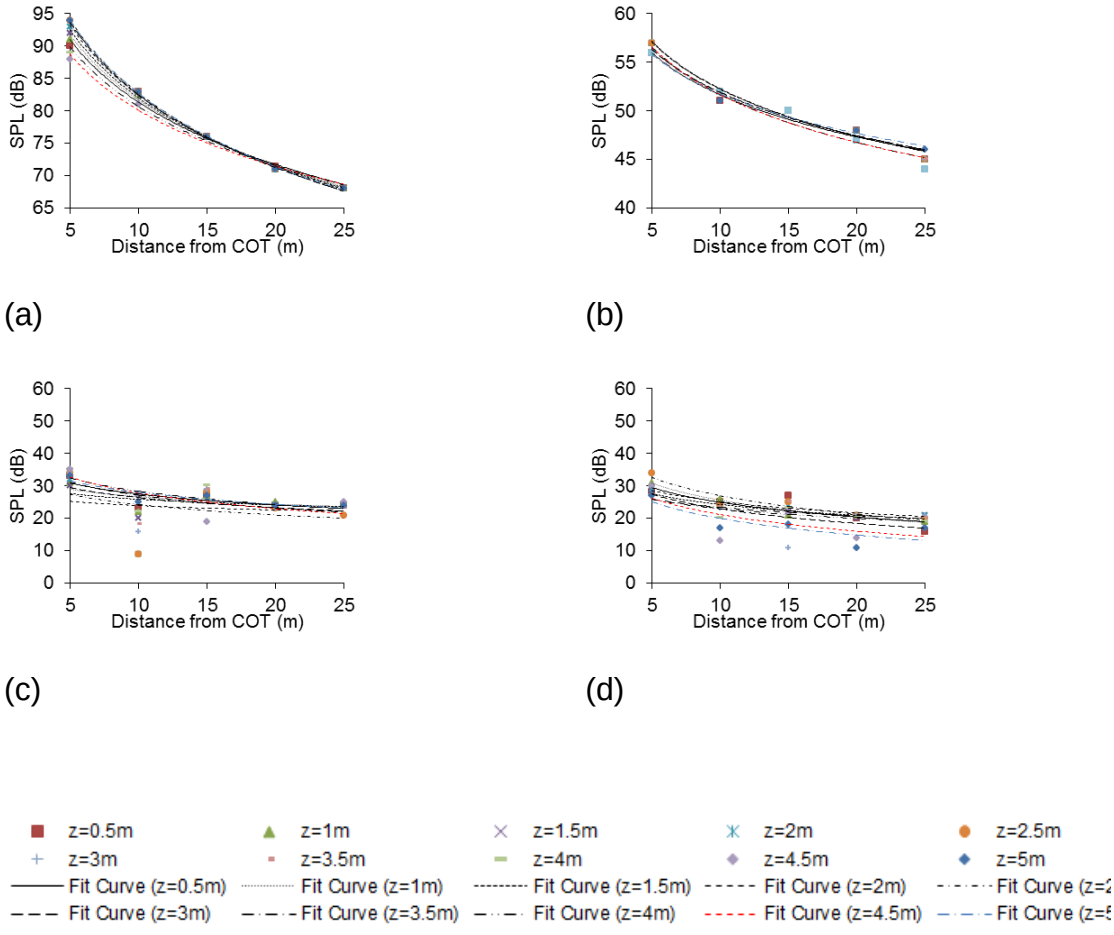

Figure 18. Effect of varying distance from COT vs. SPL (dB): (a) 12 Hz; (b) 100 Hz; (c) 1000 Hz; (d) 4000 Hz.

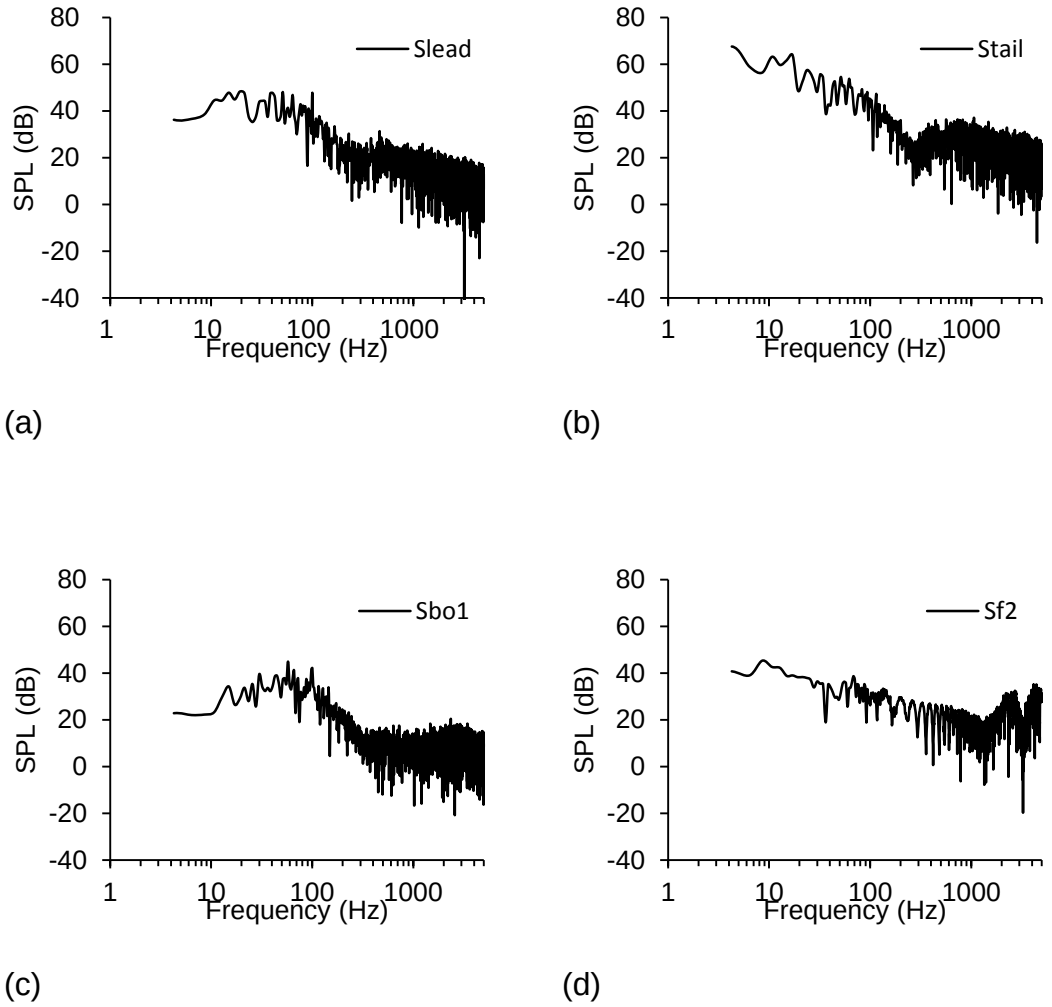

Figure 19. SPL (dB) of each integral surfaces: (a) S_{lead} (b) S_{tail}; (c) S_{bo1}; (d) $S_{f2.}$(receiver installed at (72,25,3)).

Figure 19 illustrates the SPL integrated from various surfaces on the train; tail car, which is an area of flow separation where vortices shedding into the near wake; the fairing which shield the inter-car gap between the middle car and tail car, is also a component with highly concern which is similar to the noise generated by cavity flow. In Figure 19, the SPL of the tail car is larger than lead

car. This is probably due to the measuring points installed on plane perpendicular to TOR at x=72 m from train nose, which has a smaller straight-line distance to the trail car than the lead car. The first bogie also shows typical broadband features, where tonal noise also exists at higher frequencies. The most significant SPL on a component of the high-speed train is generated by the fairing. This is illustrated as a distinct tonal noise component in accordance with Noh et al. [10].

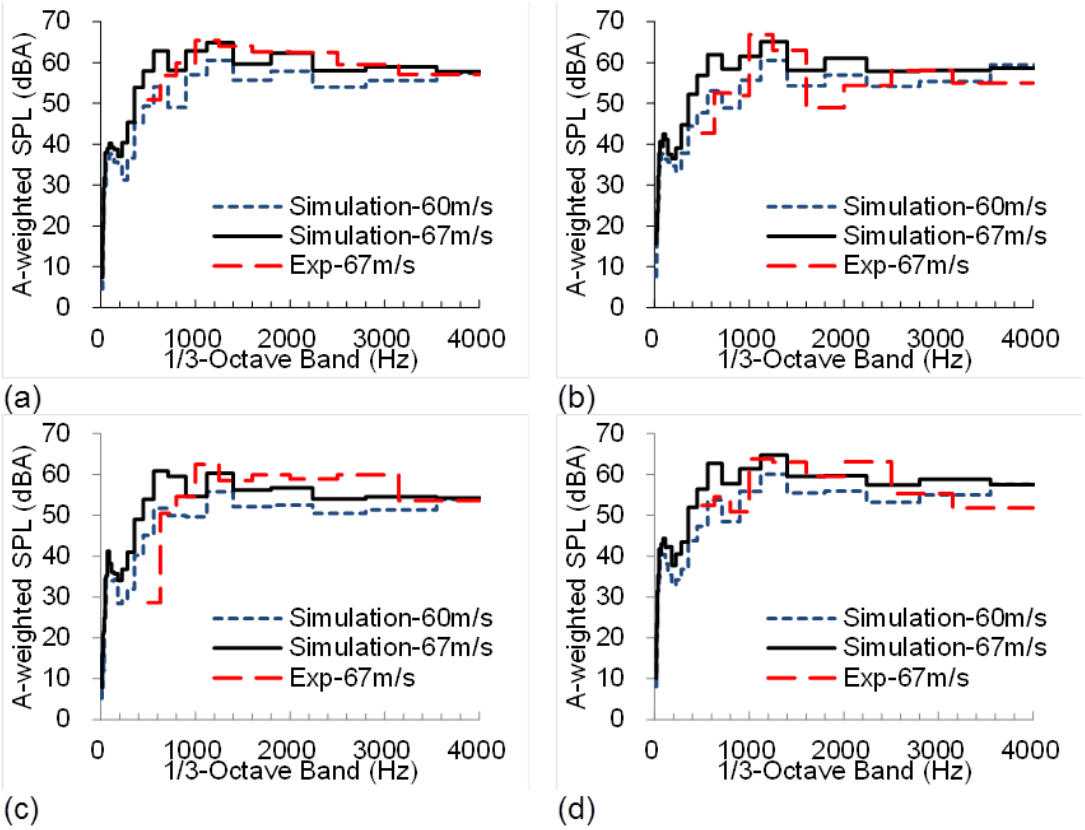

Figure 20. A-weighted SPL (dBA) at 1/3-Octave Band (Hz) at place 15 m from COT corresponding to: (a) first bogie; (b) fairing; (c) middle car; (d) tail car.

The A-weighted SPL is a filter which better reflects the actual level of sound that humans can hear because humans are not sensitive to the sounds at the lower frequencies (deep tones) and higher frequencies (high pitch).

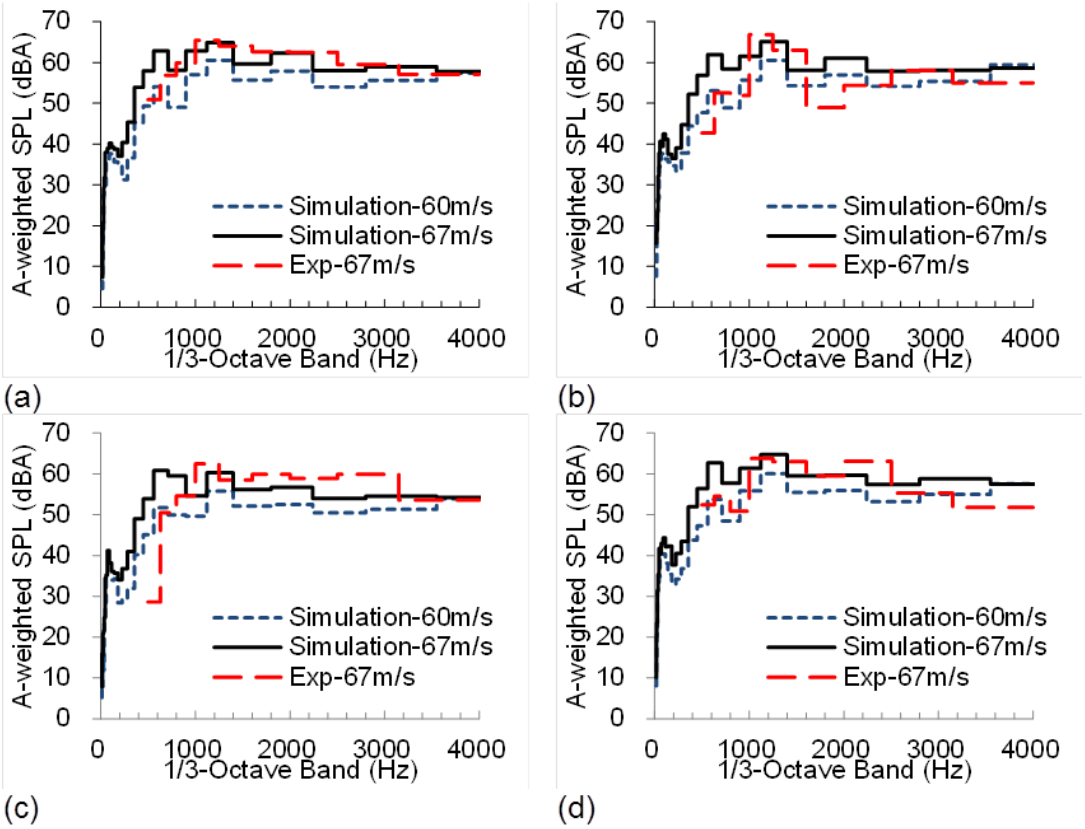

Figure 20 shows the evaluation of A-weighted SPL compared with full-scale experimental data at 15 m from COT, from which the peak value of both simulation and experiment both occur at approximately 1 kHz. The 1/3-octave band of simulation is from 14 Hz to 4 kHz, while the full-scale experiment is from 500 Hz to 4 KHz. Although results from both cases are not strictly the same, they show almost the same range of A-weighted SPL. At the described speed (60m/s, 67m/s), the acoustic source power is mainly distributed between 1 kHz to 2 kHz.

Furthermore, the peak value corresponding to each position is approximately 65 dB.

6.2 Noise source distribution

Surface acoustic power is discussed in this section to study the broadband noise source distribution, which has acoustic power that can spread across a wide range of frequencies [59]. Figure 21 shows the surface acoustic power level of all the integral surfaces. The streamlined part of the leading car accounts for the most noise of the three cars and the first bogie contributes the most noise out of the six bogies. As for the streamlined part of the leading car, the vortex shedding from the under-body complexities and the small flow structures in the boundary layer are the main noise source. Although the impact zone of boundary layer region is large, the sound intensity of boundary layer noise is always below vortex shedding noise when train speed is between 100 km/h and 500 km/h [58]. Therefore, the main contribution of the streamlined part of the lead car is vortex shedding noise, which can be seen in Figure 21(a).

Figure 21(b) shows that the leading bogie is the largest noise source among all the bogies, see both maximum and average values, (from Table 3), in accordance with the results from Nagakura 9. Lower half of the wheels are the area with strong surface noise power (dB). As shown in

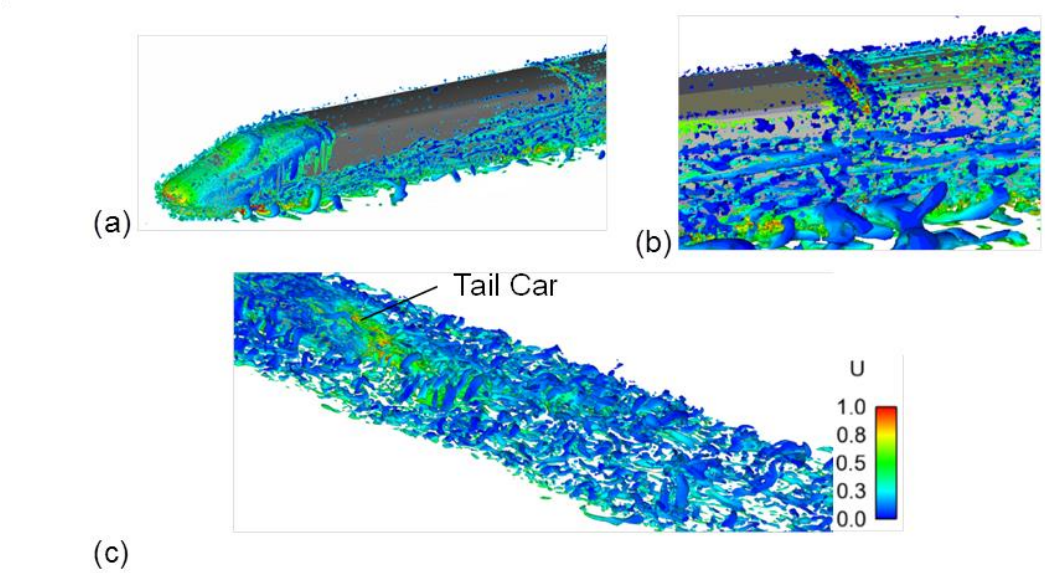

Figure 14(a), a cluster of coherent vortices generated at the bottom of leading car at the place of first bogie and extended along the train length, which illustrates the highly unsteady flow around the first bogie that can also be verified by Figure 13. First bogie experiences relatively large flow velocity compared to the other bogies. Therefore first bogie contributes the most surface acoustic power among all the other bogies.

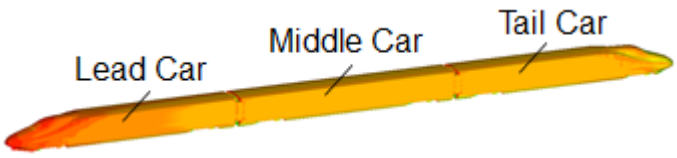

(a)

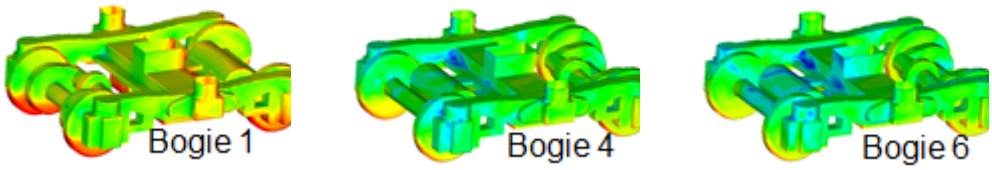

(b)

Figure 21. Surface acoustic source power distribution (dB): (a) train body; (b) bogies.

Table 3. Surface acoustic power level (dB) of maximum and average value of each part.

	S_{lead}	S_{mid}	S_{tail}	S_{bo1}	S_{bo2}	S_{bo3}	S_{bo4}	S_{bo5}	S_{bo6}	S_{f1}	S_{f2}
Ave	81.6	76.1	74.9	70.4	60.6	55.7	53.6	52.7	51.2	66.9	71.6
Max	115.2	106.4	108.1	118.0	106.9	106.0	97.3	99.0	95.2	98.5	106.0

6.3 Far-field noise directivity

Noise directivity in the far-field is an important feature of acoustic radiation, which reflects the physical feature of the sound generation mechanism [60]. Taking the train centre as the base point, measuring points are arranged every 5 degrees at a radius of 1,000 m and at a height of z=3.5m. The whole train and each bogie were selected separately as the noise source to calculate the OASPL of every measuring point for the frequency from 0 Hz to 5000 Hz. Jia et al. 61 and Moore et al. 62 took the radius of r=15D and r=30D to study the far-field noise directivity, respectively. Figure 22 shows the noise directivity of the OASPL in xy-plane at radius r=1000m, which is equal to 26D, here D is distance from train nose to train centre in horizontal plane, namely half of train length.

In Figure 22(a), the directivity of the OASPL in streamwise xy-plane indicates that the directivity of the whole train has a ‘figure of eight’ form. This is in accordance with the theoretical analysis that the main sound source of high speed train is dipole. Nevertheless, the far-field noise directivity varies due to

effects such as train shape and train speed 60. As for the train model used in this paper, the OASPL of the right-front and right-back of train is the lowest area among all the directions. However, sound emission is strongest in the direction perpendicular to the sides of the train. The directivity pattern of lead car and tail car are closely matched, where tail car is 2dB lower than the lead car at the sides of the train. In Figure 22(b), the noise directivity of OASPL integrated from surfaces of six bogies is shown. When the bogie is chosen as the noise source, the shielding effect from the bogie fairing can be neglected, since only the surface pressure fluctuations on the bogie wall surfaces are used for the resolution of FW-H acoustics analogy. Although the bogies have the same structure, the first bogie of leading train shows the strongest directivity in all directions (Figure 22(b)).

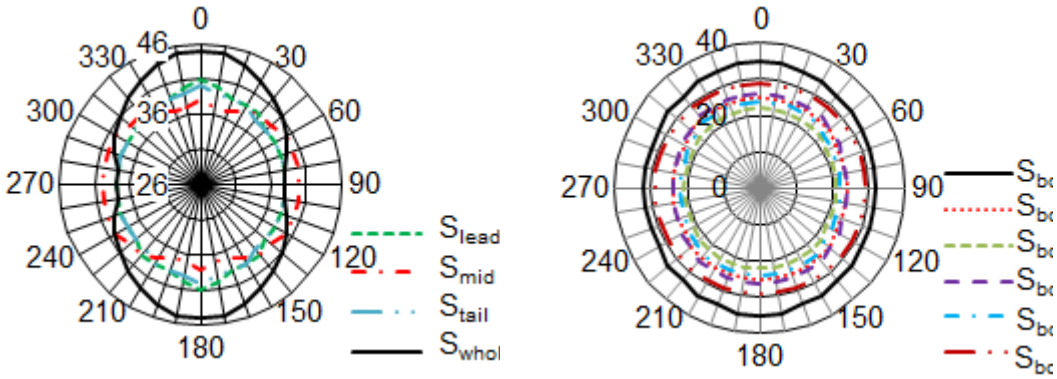

(a) (b)

Figure 22. OASPL in streamwise xy-plane of z=1.2m at radius R=26D for angles θ=0:10:360 degrees: (a) integral surfaces: each train and whole train; (b) integral surfaces: each bogie.

7. Conclusion

A hybrid DES/FW-H acoustic analogy method was used to obtain the flow and aeroacoustic fields around a 1/8th scale high speed train. Mesh sensitivity tests were conducted and the solutions were validated against force and surface pressure coefficients from wind tunnel tests. Good agreement was shown between the data sets. The slipstream was analysed using velocity, pressure coefficient, turbulence intensity and vortex visualisation. The aeroacoustic features presented were SPL, OASPL, A-weighted SPL, noise source distribution and far-field directivity. Conclusions can be drawn as follows:

(1) All simulations were well-handled by DES in that RANS is used within the boundary layer.

(2) Time-averaged drag, lift and pressure coefficient are in reasonable agreement with wind tunnel data, which are within 11%, 33% and 15%, respectively. The flow and aeroacoustics field results show some dependence on mesh density.

(3) Slipstream velocities around the train clearly shows the characteristic nose, boundary layer region, fairing and near wake regions. These regions contribute to the peak value of slipstream velocity with different distance away from COT and TOR. Nose region and near wake regions are responsible for peak slipstream velocities, whilst at lower part of train (i.e., z=0.5m), slipstream is influenced significantly by the bogies. The flow field around each bogie has also been investigated, in which leading bogie generates the highest turbulence

intensity flow.

(4) Sound propagated by a high-speed train is shown as broadband spectrum with tonal component, where SPLs are concentrated on the low frequency range (10 Hz-300Hz for this case). Fairings are the surface component which generates the most distinct tonal noise. Negative log law has been used to study the influence of distance from COT to the SPL, where a good fit is shown in lower frequencies (i.e., 12Hz, 1000Hz). Simulation results show almost the same range on items of A-weighted SPL compared with full-scale experiment, where the peak value (about 65 dB) of both is all occurs at approximately 1 kHz. At the described speed (60m/s, 67m/s), the acoustic source power is mainly distributed between 1 kHz to 2 kHz.

(5) The sound source generated by high speed train system is mainly dipole in accordance with the theoretical analysis and verified by the calculated figure of eight style noise directivity of the whole train. The leading bogie accounts for the largest broadband noise source among all the bogies by consideration of the surface acoustic power distribution and far-field directivity. This is mainly due to the highest relative velocity impacting on it compared with other bogies. Lead car is also a predominant source of broadband noise, which is mainly the vortex shedding noise.

Acknowledgement

The authors acknowledge the support of Central South University for providing the wind tunnel experimental data and full-scale experimental data.

Thanks to Dr. Zhigang Yang (Central South University) for his help on this study. The computational resources provided by the Birmingham Environment of Academic Research (BEAR) and National Supercomputer Centre in Guangzhou (China) are highly appreciated.

Funding

This work was supported by the Major Programme of the National Natural Science Foundation of China (grant number U1134203) and the National Natural Science Foundation of China (grant number 51205418).

References

1. Krajnović S. Shape optimization of high-speed trains for improved aerodynamic performance. Proc IMechE Part F: J Rail and Rapid Transit 2009; 223(5): 439-452.
2. Grosche F R, Meier G E A. Research at DLR Göttingen on bluff body aerodynamics, drag reduction by wake ventilation and active flow control. J Wind Eng Ind Aerod 2001; 89(14): 1201-1218.
3. Ito M. Improvement to the aerodynamic characteristics of Shinkansen rolling stock. Proc IMechE Part F: J Rail and Rapid Transit 2000; 214(3): 135-143.
4. Baker C, Jones J, Lopez-Calleja F, et al. Measurements of the cross wind forces on trains. J Wind Eng Ind Aerod 2004; 92(7): 547-563.
5. Bell J R, Burton D, Thompson M, et al. Wind tunnel analysis of the slipstream and wake of a high-speed train. J Wind Eng Ind Aerod 2014; 134: 122-138.
6. Zhang Z, Zhou D. Wind tunnel experiment on aerodynamic characteristic of streamline head of high speed train with different head shapes. J Cent South Univ 2013; 44(6): 2603-2608.
7. Parizet E, Hamzaoui N, Jacquemoud J. Noise assessment in a high-speed train. Appl acoust 2002; 63(10): 1109-1124.
8. Lee P J, Hong J Y, Jeon J Y. Assessment of rural soundscapes with high-speed train

noise. Sci Total Environ2014; 482: 432-439.

9. Nagakura K. Localization of aerodynamic noise source of Shinkansen trains. J Sound Vib 2006; 293(3):547-556.
10. Noh H M, Choi S, Hong S, et al. Investigation of noise sources in high-speed trains. Proc IMechE Part F: J Rail and Rapid Transit 2014; 228(3):307-322.
11. Thompson D. Railway noise and vibration: mechanisms, modelling and means of control. Elsevier, 2008.
12. Copley J. The three-dimensional flow around railway trains. J Wind Eng Ind Aerod 1987; 26(1): 21-52.
13. Baker C. The flow around high speed trains. J Wind Eng Ind Aerod 2010; 98(6): 277-298.
14. Templin J, Raimondo S. Experimental evaluation of test section boundary interference effects in road vehicle tests in wind tunnels. J Wind Eng Ind Aerod 1986; 22(2): 129-148.
15. Breuer M, Jovičić N, Mazaev K. Comparison of DES, RANS and LES for the separated flow around a flat plate at high incidence. Int J Numer Meth Eng 2003; 41(4): 357-388.
16. Hemida H, Krajnović S. LES study of the influence of the nose shape and yaw angles on flow structures around trains. J Wind Eng Ind Aerod 2010; 98(1): 34-46.
17. Krajnović S, Davidson L. Numerical study of the flow around a bus-shaped body. J Fluids Eng 2003; 125(3): 500-509.
18. Flynn D, Hemida H, Soper D, et al. Detached-eddy simulation of the slipstream of an operational freight train. J Wind Eng Ind Aerod 2014; 132: 1-12.
19. Muld T, Efraimsson G, Henningson D. Wake characteristics of high-speed trains with different lengths. Proc IMechE Part F: J Rail and Rapid Transit 2014; 228(4): 333-342.
20. Spalart P R. Detached-eddy simulation. Annu Rev Fluid Mech 2009; 41: 181-202.
21. Lateb M, Masson C, Stathopoulos T, et al. Comparison of various types of k–ε models for pollutant emissions around a two-building configuration. J Wind Eng Ind Aerod 2013; 115: 9-21.

22. Lateb M, Masson C, Stathopoulos T, et al. Simulation of near-field dispersion of pollutants using detached-eddy simulation. Comput Fluids 2014; 100: 308-320.
23. Shih T, Liou W, Shabbir A, et al. A new k-ϵ eddy viscosity model for high reynolds number turbulent flows[J]. Comput Fluids 1995; 24(3): 227-238.
24. Raghunathan R S, Kim H D, Setoguchi T. Aerodynamics of high-speed railway train. Prog Aerosp sci 2002; 38(6): 469-514.
25. Lighthill M J. On sound generated aerodynamically. I. General theory. Proc R Soc Lond A Math Phys Sci 1952; 211(1107): 564-587.
26. Fremion N, Vincent N, Jacob M, et al. Aerodynamic noise radiated by the intercoach spacing and the bogie of a high-speed train. J Sound Vib 2000; 231(3): 577-593.
27. Talotte C, Gautier P, Thompson D, et al. Identification, modelling and reduction potential of railway noise sources: a critical survey. J Sound Vib 2003; 267(3): 447-468.
28. Lauterbach A, Ehrenfried K, Kröber S, et al. Microphone array measurements on high-speed trains in wind tunnels. In: 3rd Berlin Beamforming Comference, Berlin, Germany, 24-25 February 2010, pp. 1-12.
29. Yamazaki N, Takaishi T, Toyooka M, et al. Wind tunnel tests on the control of aeroacoustic noise from high speed train. In: Noise and Vibration Mitigation for Rail Trans. Sys., NNFM 99, 2008, pp. 33-39. Springer Berlin Heidelberg.
30. Mizushima F, Takakura H, Kurita T, et al. Experimental investigation of aerodynamic noise generated by a train-car gap. J Fluid Struct 2007; 2(2): 464-479.
31. Masson E, Paradot N, Allain E. The numerical prediction of the aerodynamic noise of the TGV POS high-speed train power car. In: Noise and Vibration Mitigation for Rail Trans. Sys., NNFM 118 2012, pp. 437-444. Springer Japan.
32. Takaishi T, Sagawa A, Nagakura K, et al. Numerical analysis of dipole sound source around high speed trains. J Acoust Soc AM 2002; 111(6): 2601-2608.
33. Sun Z, Song J, An Y. Numerical simulation of aerodynamic noise generated by high speed trains. Eng Appl Comp Fluid 2012; 6(2): 173-185.

34. He B, Xiao X, Zhou Q, et al. Investigation into external noise of a high-speed train at different speeds. J Zhejiang Uni Sci A 2014; 15(12): 1019-1033.
35. Quayle A, Dowling A, Graham W, et al. Obtaining absolute acoustic spectra in an aerodynamic wind tunnel. J Sound Vib 2011; 330(10): 2249-2264.
36. Williams J, Hawkings D. Sound generation by turbulence and surfaces in arbitrary motion. Phil Trans R Soc A 1969; 264(1151): 321-342.
37. Lai H, Luo K H. A conceptual study of cavity aeroacoustics control using porous media inserts. Flow, Turbul and Combust 2008; 80(3): 375-391.
38. Gröschel E, Schröder W, Renze P, et al. Noise prediction for a turbulent jet using different hybrid methods. Comput Fluids 2008; 37(4): 414-426.
39. Luo K, Zhang S, Gao Z, et al. Large-eddy simulation and wind-tunnel measurement of aerodynamics and aeroacoustics of a horizontal-axis wind turbine. Renew Energy 2015; 77: 351-362.
40. Zhu J, Hu Z, Thompson D. Flow simulation and aerodynamic noise prediction for a high-speed train wheelset. Int J Aeroacousti 2014; 13(7-8): 533-552.
41. Yu H H, Li J C, Zhang H Q. On aerodynamic noises radiated by the pantograph system of high-speed trains. Acta Mech Sinica 2013; 29(3): 399-410.
42. ANSYS FLUENT Documentations. http://aerojet.engr.ucdavis.edu/fluenthelp/html/ug/node1513.htm (2015, accessed 1 October 2015)
43. Syed S A, Hoffmann K A. Detached Eddy Simulation of Turbulent Flow over a Partially Open Cavity. In: 28th AIAA Applied Aerodynamics Conference Chicago, America, 28 June- 1 July 2010, pp.5072. AIAA Paper 2010.
44. Thompson D J, Latorre Iglesias E, Liu X, et al. Recent developments in the prediction and control of aerodynamic noise from high-speed trains. Int J Rail Trans 2015; 3(3): 119-150.
45. Di Francescantonio P. A new boundary integral formulation for the prediction of sound

radiation. J Sound Vib 1997; 202(4): 491-509.
46. Liu J Z, Li R X, Cui P X. Numerical Analysis of the Surface Aerodynamic Noise of the CRH3 High Speed Train. Adv Mater Res 2014; 1044: 643-649.
47. Goldstein M E. Aeroacoustics. New York: McGraw-Hill International Book Co., 1976.
48. Schober M, Weise M, Orellano A, et al. Wind tunnel investigation of an ICE 3 endcar on three standard ground scenarios. J Wind Eng Ind Aerod 2010; 98(6): 345-352.
49. EN 14067-6:2010. Railway applications-Aerodynamics-Part 6: requirements and test procedures for cross wind assessment.
50. Mendez S, Shoeybi M, Lele S, et al. On the use of the Ffowcs Williams-Hawkings equation to predicted far-field jet noise from large-eddy simulations. Int J Aeroacousti 2013; 12(1-2): 1-20.
51. EN 14067-4:2005. Railway applications-Aerodynamics-Part 4: requirements and test procedures for aerodynamics on open track.
52. Hemida H, Bake C, Gao G. The calculation of train slipstreams using large-eddy simulation. Proc IMechE Part F: J Rail and Rapid Transit 2012: 228(1):25-36.
53. Sterling M, Baker C, Jordan S, et al. A study of the slipstreams of high-speed passenger trains and freight trains. Proc IMechE Part F: J Rail and Rapid Transit 2008; 222(2): 177-193.
54. Pope S B. Turbulent flows. Cambridge university press, 2000.
55. Viola I M, Bartesaghi S, Van-Renterghem T, et al. Detached Eddy Simulation of a sailing yacht. Ocean Eng 2014; 90: 93-103.
56. ISO EN 3095: 2005. Railway applications–acoustics–measurement of noise emitted by railbound vehicles.
57. Fahy F, Walker J. Fundamentals of noise and vibrations. CRC Press, 1998, p.145-148.
58. Rathe E J. Note on two common problems of sound propagation. J Sound Vib 1969; 10(3):472-479.
59. Murphy E, King E. Environmental Noise Pollution: Noise Mapping, Public Health, and

Policy. Newnes, 2014, p. 16-18.

60. Zhang X, Jonasson H G. Directivity of railway noise sources. J Sound Vib 2006, 293(3): 995-1006.

61. Jia S H, Yang B, Zhao X L, et al. Numerical simulation of far field acoustics of an airfoil using vortex method and 2-D FW-H equation. IOP Conference Series: Material Science and Engineering. IOP Publishing, 2013, 52(2):449-463.

62. Moore P, Slot H, Boersma B J. Simulation and measurement of flow generated noise. J Comput Phys 2007; 224(1): 449-463.